

ARTICLE OPEN



Inhibition of the localised corrosion of AA2024 in chloride solution by 2-mercaptobenzimidazole and octylphosphonic acid

Dževad K. Kozlica^{1,2}, Javier Izquierdo^{3,4}, Ricardo M. Souto^{3,4} and Ingrid Milošev¹

The scanning vibrating electrode technique was employed to monitor the in situ localised electrochemical activity on aluminium alloy 2024-T3 at the free corrosion potential in aggressive NaCl solutions with and without corrosion inhibitors 2-mercaptobenzimidazole (MBI) and octylphosphonic acid (OPA). MBI is a very effective inhibitor against pitting corrosion, even in a chloride environment without the reservoir of MBI. In contrast, localised corrosion was observed at several points at the early stage of immersion of AA2024 in NaCl solution containing OPA. Ex situ energy-dispersive X-ray spectroscopy analysis of the Al₂CuMg particle at the cross-section revealed that MBI does not entirely prevent its dissolution but reduces the dissolution rate and the rate of oxygen reduction by forming an insoluble complex compound Cu–MBI on the partially dealloyed AlCu-based particles, i.e., on the porous copper remnants. The MBI's action is an efficient option for mitigating the corrosion of Cu-based aluminium alloys.

npj Materials Degradation (2023)7:55; <https://doi.org/10.1038/s41529-023-00368-z>

INTRODUCTION

High strength-to-weight ratio aluminium alloy (AA) 2024-T3 is an indispensable material in many transport industries like aerospace as it increases loading capacity and reduces energy consumption¹. Although nano-to-micro scale intermetallic particles (IMPs) are the main contributors to mechanical properties, they are also the main culprits for the most insidious site-specific local degradation events at the surface of AA2024². IMPs such as Al₂CuMg and Al₂Cu tend to dealloy at the open circuit potential (OCP), leading to the creation of catalytic high surface area copper enriched intermetallic remnants and associated copper redistribution (i.e., copper replating) on the alloy surface^{3–8}. Both of these processes significantly support increased oxygen reduction reaction (ORR) rates leading to increased local alkalinity due to the production of OH[−] ions, causing aluminium matrix dissolution in the form of localised trenching around the IMPs and pit initiation and growth^{9–11}. Therefore, an effective way to increase the corrosion resistance of AA2024 is to suppress the dissolution of IMPs. One aspect of current research in corrosion inhibition has focused on organic molecules with heteroatoms, such as nitrogen, oxygen, sulphur and phosphorus, that contain a lone pair of electrons and/or delocalised π electrons due to the presence of multiple bonds or aromatic rings¹².

Our research group recently evaluated, using conventional electrochemical techniques, the efficacy of 2-mercaptobenzimidazole (MBI) and octylphosphonic acid (OPA) as single inhibitors¹³ and their mixtures to achieve possible synergy¹⁴ on copper and aluminium. MBI is an efficient inhibitor of copper corrosion due to its adsorption as deprotonated thiolate and the formation of a stable inhibitor film with the copper surface^{13,14}. OPA, on the other hand, does not form strong bonds with Cu, but it forms strong metal-phosphonate bonds with Al^{13,14}. Therefore, the MBI is an efficient inhibitor for Cu but not for Al, and OPA shows just the opposite behaviour in relation to Cu and Al substrates. These

two compounds show a strong synergistic effect on Cu; when used in a molar mixture MBI: OPA = 9 : 1, a bonding mechanism changes from thiolate to thionate and thione forms of MBI¹⁴. Furthermore, a thicker inhibitor film was formed owing to the change in pH to a slightly acidic range where the formation of cuprous ions is stimulated. It was discovered that chloride ions, acting simultaneously as promoters and reactants in forming a thick inhibitory film on copper¹⁵, caused the establishment of the aforementioned synergistic effect. No synergy of MBI and OPA was observed on aluminium, but MBI did not obstruct the inhibitor action of OPA, which is a good inhibitor for Al corrosion¹⁴. These previous results were the starting points for the next step of the research hypothesising that MBI and OPA would act complementary on Cu-rich IMPs and Al matrix, respectively, and thus mitigate the corrosion of AA2024.

The classical electrochemical techniques provide limited information on the electrochemical behaviour at corrosion initiation sites and lack sufficient spatial resolution (i.e., they only provide information on the corrosion rates averaged over the entire surface). Thus, we used localised electrochemical research techniques which offer in situ monitoring of the electrochemical activity at an early stage of corrosion and the progression of corrosion processes with time, with and without the presence of inhibitors^{16,17}. Firstly, scanning electrochemical microscopy (SECM) and scanning vibrating electrode technique (SVET) were explored to study the Al/Cu galvanic pair in chloride solution and discern local anodic and cathodic sites¹⁸. The electrochemical activity in the galvanic pair was greatly reduced when the Cu surface was covered by MBI, thus blocking the cathodic sites¹⁸. In contrast, OPA did not provide sufficient barrier properties against the penetration of chloride ions and did not prevent pitting corrosion¹⁸. Continuing our approach further and translating to the AA2024 Cu-rich Al alloy, we have focused here on a localised

¹Jožef Stefan Institute, Department of Physical and Organic Chemistry, 1000 Ljubljana, Slovenia. ²Jožef Stefan International Postgraduate School, 1000 Ljubljana, Slovenia.

³Department of Chemistry, Universidad de La Laguna, 38200 La Laguna, Tenerife, Spain. ⁴Institute of Material Science and Nanotechnology, Universidad de La Laguna, 38200 La Laguna, Tenerife, Spain. ✉email: rsouto@ull.es; ingrid.milosev@ijs.si

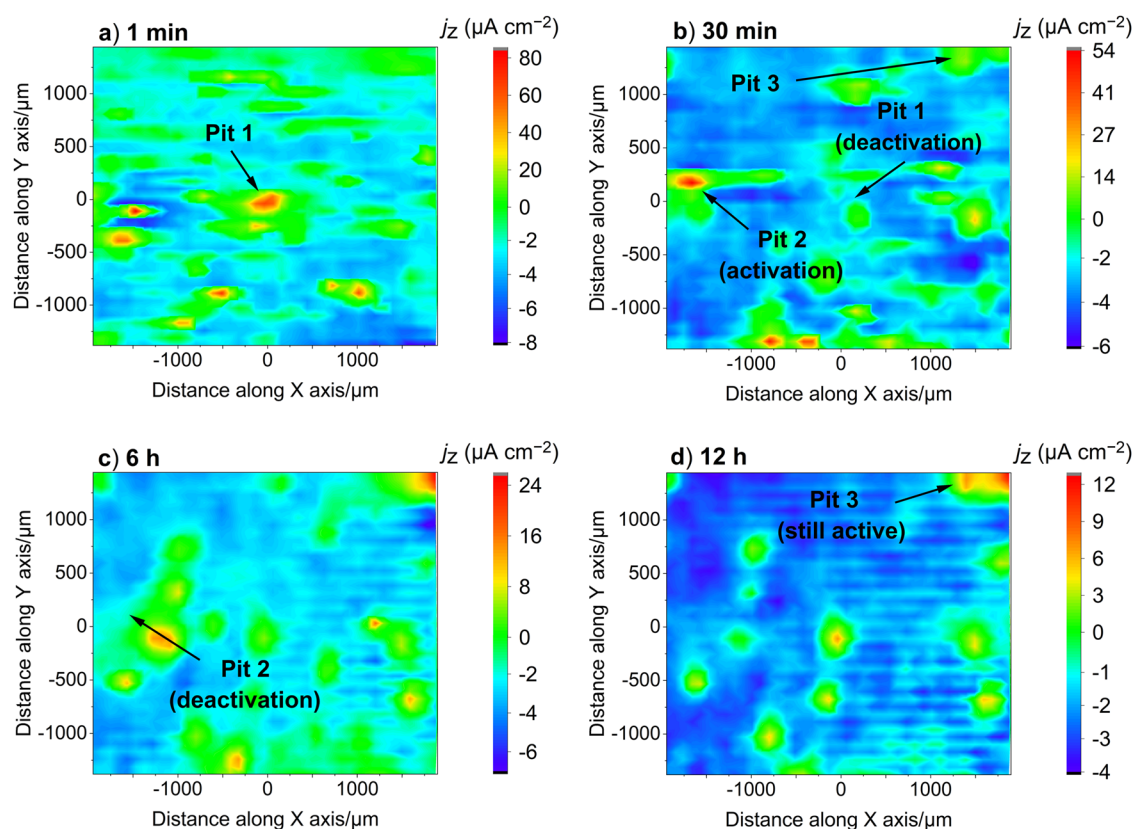


Fig. 1 SVET maps of AA2024 in NaCl. SVET maps recorded over AA2024 during immersion in 10 mM NaCl at selected exposure times: **a** 1 min, **b** 30 min, **c** 6 h and **d** 12 h. Areas of positive (anodic) and negative (cathodic) ionic current densities are given according to the colour scale bars from red to blue, respectively. Some pits (denoted by the red colour of high anodic current densities) tend to disappear at longer immersion time.

microelectrochemical approach using the SVET to study the actions of organic compounds MBI and OPA.

Numerous localised electrochemical studies on corrosion inhibition of AA2024 were reported. Lamaka et al.¹⁹ showed, by applying the scanning Kelvin probe force microscopy (SKPFM), that quinaldic acid, salicylaldehyde and 8-hydroxyquinoline (8-HQ) suppress the dissolution of Mg, Al and Cu from intermetallic particles. Marcelin and P  b  re²⁰ investigated the 8-HQ and benzotriazole (BTA) mixture on Al/Cu couple and AA2024 by localised electrochemical impedance spectroscopy (LEIS). The corrosion inhibition effect of BTA was mainly limited to the copper-rich IMPs, whereas 8-HQ acted on the Al matrix due to its chelating properties. Williams et al.²¹ used SVET to quantify the effect of several copper complexing/precipitation reagents on the kinetics of pitting corrosion. The results showed that 2,5-dimercapto-1,3,4-thiadiazolate (DMTD), BTA and N,N-diethyl-dithiocarbamate (DEDTC) effectively inhibit pitting corrosion by the formation of a metal-inhibitor film on Cu-rich IMPs. In addition, they revealed that ethylenediaminetetraacetic acid (EDTA) prevented Cu replating without decreasing localised corrosion currents. This finding suggests sufficient cathodic oxygen reduction can be sustained on Cu-rich and dealloyed IMPs to drive the observed pitting corrosion without any copper replating. Cross-sectional analytical transmission and scanning electron microscopies were used to reveal a dealloying-driven local corrosion initiation at the studied IMPs that have been considered as cathodic phases traditionally (such as Al₇Cu₂Fe(Mn)), thus suggesting a possible initial (local) anodic character in most IMPs due to local compositional variations^{22,23}. Independently, Olgjati²⁴

showed that dealloying of the S-phase occurs twice as fast as the dealloying of AlCuFeMn.

Based on previously shown individual and synergistic inhibition actions of MBI and OPA on Cu and Al metals^{13–15,18}, this paper is devoted to exploring the detailed interaction mechanism of MBI and OPA, as potential corrosion inhibitors for aluminium alloy 2024, with different Al- and Cu-rich intermetallic particles. The local electrochemical activity was evaluated in situ and quasi-real-time using SVET at the free corrosion potential in an inhibitor containing aggressive electrolyte such as 10 mM NaCl. Conventional electrochemical characterisation by potentiodynamic polarisation was performed in 0.5 M NaCl. Here, we also sought to understand the viability of formed inhibitory films and their effectiveness against corrosion in the NaCl solution that does not contain an MBI or OPA reservoir. Finally, we attempted to provide a more comprehensive morphological and surface chemical composition, both on top and cross-section of the substrate, using ex-situ focused ion beam/scanning electron microscopy coupled with energy-dispersive X-ray spectroscopy (FIB-SEM-EDS).

RESULTS AND DISCUSSION

Localised activity of AA2024 in chloride solution

The visualisation of ionic current flows was determined by repetitive in situ SVET scanning as a function of time over the surface of an unpolarised AA2024 sample, corroding freely in an aerated 10 mM NaCl solution without added inhibitor. Less concentrated solutions were selected for SVET measurements compared to polarisation curves and SEM-EDS experiments (where 0.5 M NaCl was chosen) because the sensitivity of SVET

for measuring ionic current density is compromised by high electrolytic conductivity. Figure 1 shows representative ionic current density maps taken immediately after immersion (i.e., after 1 min), after 30 min, 6 h and 12 h. In the interests of better spatial resolution of the distribution of electrochemical activity on the surface of the AA2024, where the small IMPs concentrate the anodic activity while the corresponding cathodic activity is distributed over the larger matrix alloy, SVET images are constructed using two different scales; one is employed for the highly localised positive ionic (anodic) current densities and another for the more homogeneously distributed negative ionic (cathodic) current density distributions over the larger alloy matrix. An SVET scan recorded immediately after immersion revealed local anodic activity at numerous locations with a maximum ionic current density of $j_z \leq 85 \mu\text{A cm}^{-2}$, indicating that localised corrosion begins within 1 min of exposure to the chloride-containing solution (Fig. 1a). The observed positive ionic currents are due to the flux of Al^{3+} ions released from the IMPs due to dealloying in the presence of chloride ions. Apart from the dealloying of the IMPs, the dissolution of the Al matrix at the periphery of the IMPs could also contribute to positive ionic currents, leading to pit initiation and growth. Successive scans show that some individual pits propagated and remained active over 12 h. In contrast, many others tended to deactivate or even became passive, which is observable by a reduced magnitude of the ionic current densities in the latter case (Fig. 1a–d). These changes with immersion time are related to the stochastic nature of the pitting process, including different stages such as pit nucleation, initiation, metastable regime, and stable pit growth^{2,25}. Some nucleated pits do not propagate but re-passivate^{2,25}.

The visual appearance of the sample surface after 1 min and at the end of the immersion period of 12 h is shown in Fig. 2. The pit openings that coincide with the locations of the high anodic ionic current densities were especially pronounced during prolonged immersion; however, the ionic current densities decrease, which can be attributed to the deposition of corrosion products over time and changed electrochemical activity of some IMPs during immersion. Whilst each pit can be considered a point anode, the cathodic reaction, which is assumed to be the ORR, takes place in the surrounding areas (Fig. 1). It is likely that due to the excessive copper redistribution around the pit openings, as well as on the greater part of the surface of the Al matrix, new cathodic sites are formed over time. This process stimulates even more intensive oxygen reduction, reflected in more pronounced cathodic ion fluxes (i.e., negative ionic current densities) (Fig. 1a, d). It should be noted that the pits shown in Fig. 2b are much larger in size compared to the pits in Fig. 2a due to the increase in local alkalinity resulting from the generation of OH^- ions during oxygen reduction at the cathodic sites, which causes increased dissolution of the surrounding matrix at the periphery of the Cu-containing IMPs leading to localised corrosion and trenching²³. One promising strategy to increase the corrosion resistance of AA2024 is to suppress the selective dissolution of Cu-rich IMPs (e.g., S-phase). For this purpose, the effectiveness of two corrosion inhibitors, MBI and OPA, in mitigating the pitting corrosion of AA2024 was evaluated.

Localised corrosion inhibition of AA2024 in MBI-containing solution

Figure 3 shows the maps of the ionic current density distributed over the surface of an AA2024 sample corroding spontaneously at the free corrosion potential during in situ immersion in a solution containing MBI (i.e., 10 mM NaCl + 1 mM MBI). An ionic current density map taken immediately after immersion (i.e., after 1 min) did not reveal significant local electrochemical activity indicating that the MBI inhibitor is instantly very effective against pitting corrosion (Fig. 3a). Ionic currents were homogeneously distributed

over the sample surface with extremely low values. After 24 h immersion, an additional decrease in the ionic current density was observed, with anodic activity $j_z \leq 0.5 \mu\text{A cm}^{-2}$, which may be a consequence of preventing the dissolution of S-phase particles since the MBI is a well-known inhibitor for Cu^{26–32} (Fig. 3b). The visual appearance of the sample surface after 1 min and 12 h of immersion is shown in Supplementary Fig. 1a, b. After that, the cell was rapidly washed with distilled water to remove traces of inhibitor and then filled with 10 mM NaCl solution to define its effectiveness against corrosion in a chloride environment without an MBI reservoir. In the early phase of immersion in NaCl solution (i.e., after 1 min) (Fig. 3c), one localised anodic site with activity not exceeding $5 \mu\text{A cm}^{-2}$ was observed, which was deactivated after 12 h (Fig. 3d). The visual appearance of the sample surface is shown in Supplementary Fig. 1c, d. Meanwhile, the remaining sample surface was slightly active due to the reported cathodic ionic current densities ($j_z \leq -4.5 \mu\text{A cm}^{-2}$ in Fig. 3c) originating from the reduction of dissolved oxygen. This implies moderate retention of inhibitory properties in the environment without MBI. We have previously reported that MBI adsorbs only on Cu but not on Al^{13,14,18}. Therefore, we assume here for AA2024 that the Cu-MBI film is formed on Cu-containing IMPs in the MBI solution. The Cu-MBI film provides significant in situ protection of the alloy substrate even after being removed from the MBI inhibitor solution, i.e., inhibitor reservoir, and replaced with only aggressive NaCl solution. Compared to Fig. 1, where the ionic currents in 10 mM NaCl solution could reach $85 \mu\text{A cm}^{-2}$, in Fig. 3c, d the exposure of AA2024 surface to MBI solution for 24 h before immersion in inhibitor-free NaCl solution hampered the localised activity to exceed over $5 \mu\text{A cm}^{-2}$ due to the stable Cu-MBI film, which prevented or diminished the dealloying of IMPs.

Localised corrosion inhibition of AA2024 in OPA-containing solution

In contrast to the MBI inhibitor treatment, when AA2024 was exposed to a solution containing the OPA inhibitor (i.e., in 10 mM NaCl + 1 mM OPA), localised corrosion was observed at several spots at a very early stage of immersion with an anodic ionic current density of $28 \mu\text{A cm}^{-2}$ (Fig. 4). The optical micrographs of the sample surface after 1 min and 24 h of immersion are shown in Supplementary Fig. 2. The anodic activity increased dramatically during prolonged immersion (i.e., after 24 h, $j_z \leq 180 \mu\text{A cm}^{-2}$). Interestingly, cathodic ionic currents were perhaps very weak over the entire surface but significantly increased near the pits, indicating that OPA is a good inhibitor for the Al matrix but does not prevent pitting corrosion. Due to the appearance of pitting in the presence of OPA, further experiments in NaCl solution without an OPA reservoir were not conducted.

Conventional polarisation measurements

Figure 5 shows the anodic and cathodic polarisation curves for AA2024 (i.e. blank or control sample) after 24 h ex-situ immersion in 0.5 M NaCl solution with and without adding 1 mM MBI or OPA. Measurements were performed in a classical (macro)-electrochemical set-up using the AA2024 surface as the working electrode. Deduced electrochemical parameters are given in Supplementary Table 1. The cathodic ionic current densities of the sample in the presence of MBI are reduced for more than one decade together with the lower value of the cathodic Tafel slope ($-b_c = 193 \text{ mV dec}^{-1}$), compared to the blank ($-b_c = 307 \text{ mV dec}^{-1}$). In addition, little to no anodic inhibition was observed despite the shift of E_{corr} to more positive values. This indicates that MBI is an effective cathodic corrosion inhibitor for AA2024 in an aqueous electrolyte containing chloride ions, resulting in the creation of a cathodically controlled system through the chemisorption of MBI-inhibitor molecules to the substrate (IMPs) via S and/or N atom(s), thus reducing the corrosion rates^{13–15,18}. In contrast, the OPA sample

has no corrosion inhibitor characteristics, i.e., it neither affects cathodic (especially on ORR kinetics) nor anodic reactions. The polarisation curves measurements are consistent with SVET results, except that the lack of anodic activity observed in SVET can be attributed either to significantly lower NaCl concentrations (10 mM) compared to polarisation curves experiments (0.5 M) or to the fact that the localised corrosion is highly stochastic and difficult to measure.

Surface characterisation

Ex-situ surface analysis of AA2024 was performed by SEM-EDS after 24 h of immersion in 0.5 M NaCl electrolyte with and without added MBI or OPA (Fig. 6). The surface of the control sample (i.e., in NaCl solution without inhibitor) showed drastic changes due to localised corrosion processes, possibly, including Cu deposits over the entire surface of the Al matrix originating from the well-known copper redistribution process⁴ (Fig. 6a). This behaviour aligns with

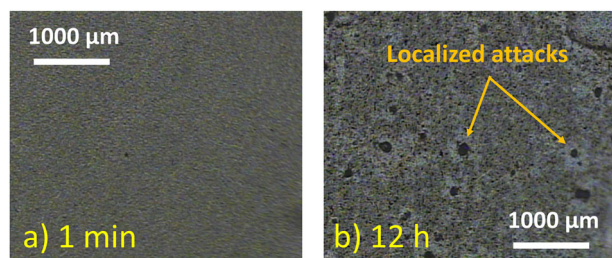


Fig. 2 Optical micrographs of AA2024 in NaCl. Optical micrographs corresponding to the SVET images given in Fig. 1a, d.

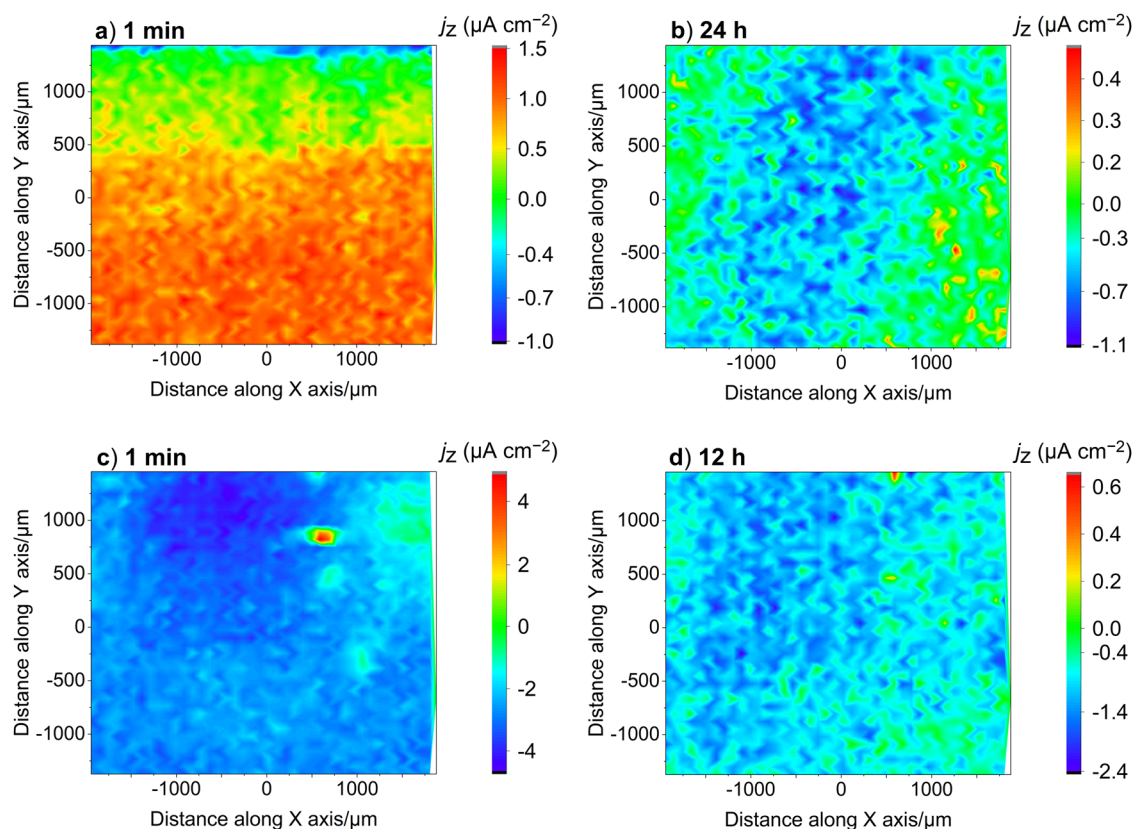


Fig. 3 Ionic current maps of AA2024 in NaCl + MBI. Ionic current density maps recorded above an AA2024 during immersion in 1 mM MBI + 10 mM NaCl at selected exposure times: **a** 1 min and **b** 24 h. The inhibitor solution was then replaced with 10 mM NaCl, and the maps were taken after **c** 1 min and **d** 12 h immersion. Areas of positive and negative ionic current densities are given according to the colour scale bars from red to blue, respectively. Optical micrographs corresponding to the SVET images are given in Supplementary Fig. 1.

the proposed dealloying mechanism of S-phase producing predominantly Cu metal particles that are no longer attached to the metal surface and are mobile under the influence of moving solution or corrosion product^{3,4}.

The sample pretreated with the MBI inhibitor had an insignificant number of these Cu deposits (Fig. 6b). This may imply that MBI inhibits the dealloying of IMPs and thus prevents copper redistribution or mitigates corrosion of Cu remnants. Both strategies would lead to an improvement in the kinetics of cathodic activity at local sites. In contrast, Fig. 6c shows that the OPA acted as a corrosion activator, resulting in many Cu particles surrounding the dealloyed IMPs.

The SEM images of the denoted area in Fig. 6a are recorded at higher magnification in SE and BSE modes (Fig. 7). Related EDS elemental maps and point analysis provide information on the elemental distribution after corrosion attack in NaCl solution without inhibitor (Fig. 7 and Table 1). There was evidence of a relatively high Cu content due to preferential dealloying of Al and Mg in the particle and dissolution of the Al matrix, which subsequently caused trenching around these particles. Semi-quantitative EDS chemical analysis of bare AA2024 (i.e. sample before immersion in NaCl solution) is shown in Supplementary Fig. 3 for comparison. It reveals that after immersion, the concentrations of Al and Mg are largely reduced due to dealloying. Further, the high O counts around the particle may indicate a thicker oxide than the surrounding matrix (Table 1).

For the sample treated with MBI, the EDS elemental maps (Fig. 8) show the distribution of S and N, which are an integral part of MBI. This suggests that MBI molecules form precipitates on copper-rich intermetallic particles via stable Cu-S and Cu-N bonds, thus blocking ORR sites, as previously shown using XPS

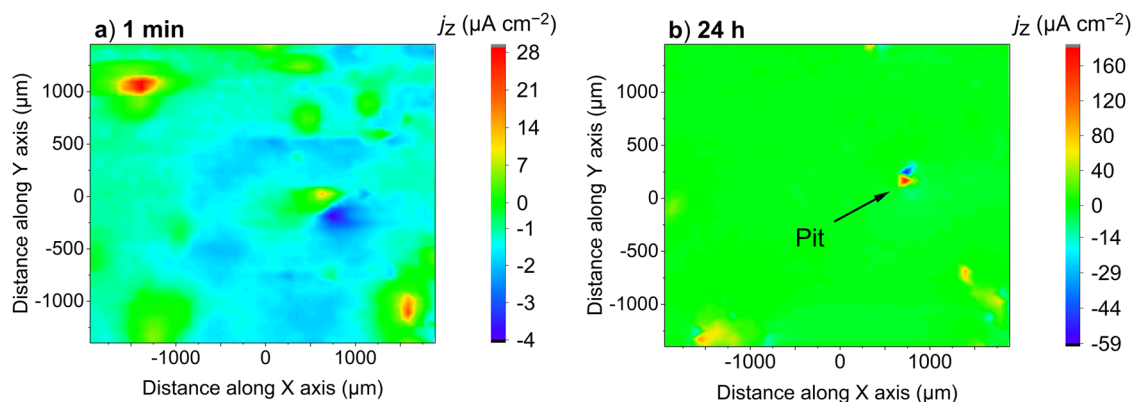


Fig. 4 Ionic current maps of AA2024 in NaCl + OPA. Ionic current density maps recorded above an AA2024 during immersion in 1 mM OPA + 10 mM NaCl at selected exposure times: **a** 1 min and **b** 24 h. Areas of positive and negative ionic current densities are given according to the colour scale bars from red to blue, respectively. Optical micrographs corresponding to the SVET images are given in Supplementary Fig. 2.

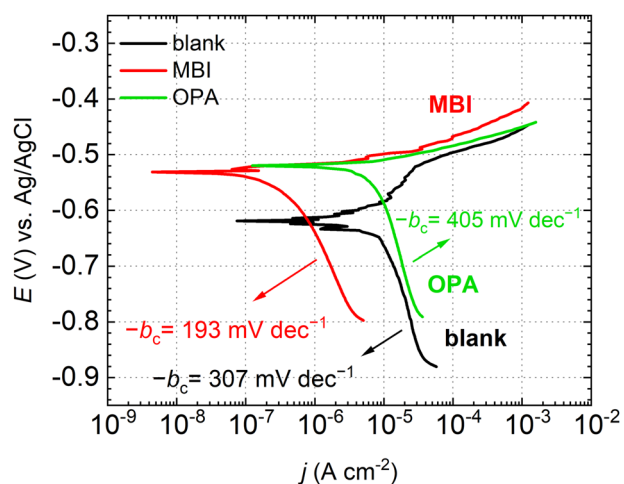


Fig. 5 Potentiodynamic polarisation curves of AA2024 in NaCl with and without MBI and OPA. Surface-averaging polarisation curves recorded for AA2024 after 24 h immersion in 0.5 M NaCl solution with and without adding 1 mM of MBI or OPA. The scan rate was 1 mV s^{-1} . The b_c values represent the corresponding cathodic Tafel slopes. Deduced electrochemical parameters are given in Supplementary Table 1.

and DFT^{14,29,30}. In contrast, MBI was not precipitated on the Al matrix (Fig. 8, location 5, Table 2), consistent with our previous observations on a bare aluminium surface¹³. However, the detected sulphur at location 5 indicates the presence of MBI, most likely on Cu domains in solid solution, but this is negligible. It should be emphasised that the copper/iron-rich IMP (most likely $\text{Al}_7\text{Cu}_2\text{Fe}(\text{Mn})$) was significantly attacked but still not completely dealloyed due to the remaining Al in the particle (locations 3 and 4, Table 2) and the lack of a bright ring around the particle corresponding to O counts, i.e., oxide deposits. MBI was also detected on the S-phase (Al_2CuMg) particle as shown in Supplementary Fig. 3.

The cross-section shown in Fig. 9 determines the dealloying penetration depth of the S-phase particle of Supplementary Fig. 4. The preferentially attacked particle resulted in a spongy morphology of the dealloyed S-phase with a continuous solid network of Cu-enriched remnants. Cross-sectional EDS analysis of the S-phase particle revealed that dissolution gradually evolved from the surface inwards. However, the remaining Mg with significant amounts of S and N (Fig. 9, locations 4 and 5, Table 3) indicates that the Al_2CuMg was not completely corroded because MBI

adsorbed on the porous copper surface resulting from the dealloyed S-phase particle. Likely, MBI does not entirely prevent S-phase dissolution. Still, it does reduce the dissolution rate and the rate of oxygen reduction on the porous copper remnant, as shown by potentiodynamic polarisation measurements (cf. Figure 5). Therefore, this behaviour is believed to be similar to the interaction of MBI with bare copper^{13,14}. It is interesting that chlorine is observed where S and N are detected (Table 3, Supplementary Fig. 4), which is consistent with our recent finding¹⁵, where the role of chloride ions in the formation of corrosion protective films on copper is described in detail.

On the other hand, the S-phase of the OPA-treated sample is characterised by complete corrosion where Al and Mg are selectively dissolved in the first stage, leaving the Cu-rich remnants exposed to the corrosion environment (Fig. 10). The IMP is almost entirely dealloyed and undercut from its adjacent matrix. EDS point analysis showed that copper redistribution occurs in the IMP environment, i.e., that redeposited Cu particles are trapped within the oxide deposit around the intermetallics (Fig. 10, locations 3 and 4, Table 4). In addition, the phosphorus map showed that OPA has not adsorbed on the IMP or Cu remnant but only on the Al matrix (Fig. 10, locations 3, 4 and 5, Table 4), which is consistent with the preference for OPA to readily form bonds with aluminium, but not with Cu. However, the adsorption of OPA was not sufficient to alleviate the local dissolution of AA2024. Our previous study on Al metal showed that phosphonic acids act as strong inhibitors of Al corrosion³³. The prolongation of the alkyl chain from eight to eighteen carbon atoms further increases the inhibitory action of the phosphonic group³³. Further study to reveal the effect of increased concentrations of OPA and/or prolonged chain lengths of phosphonic acids in the case of AA2024 remains to be continued.

In summary, MBI is a very effective cathodic inhibitor for AA2024 in a chloride medium, exhibiting a lower cathodic Tafel slope ($-b_c = 193 \text{ mV dec}^{-1}$) than the blank ($-b_c = 307 \text{ mV dec}^{-1}$). In addition, SVET showed no localised activity on AA2024, even in a chloride environment without added MBI. On the other hand, OPA induces localised corrosion of AA2024, and its cathodic Tafel slope ($-b_c = 405 \text{ mV dec}^{-1}$) is higher than that of the control sample, indicating higher kinetics of the cathodic reaction (particularly the ORR). Qualitative EDS analysis at the cross-section revealed that MBI does not entirely prevent the dealloying of Al and Mg, but reduces the dissolution rate and the rate of oxygen reduction by forming an insoluble Cu-MBI film on the partially dealloyed AlCu-based particles, i.e., on the porous copper remnants. Therefore, MBI has the potential to be used as a corrosion inhibitor of Cu-based aluminium alloys, while OPA, although it acts inhibitory on Al matrix, is a corrosion activator of Cu-rich sites leading to the propagation of localised corrosion. This

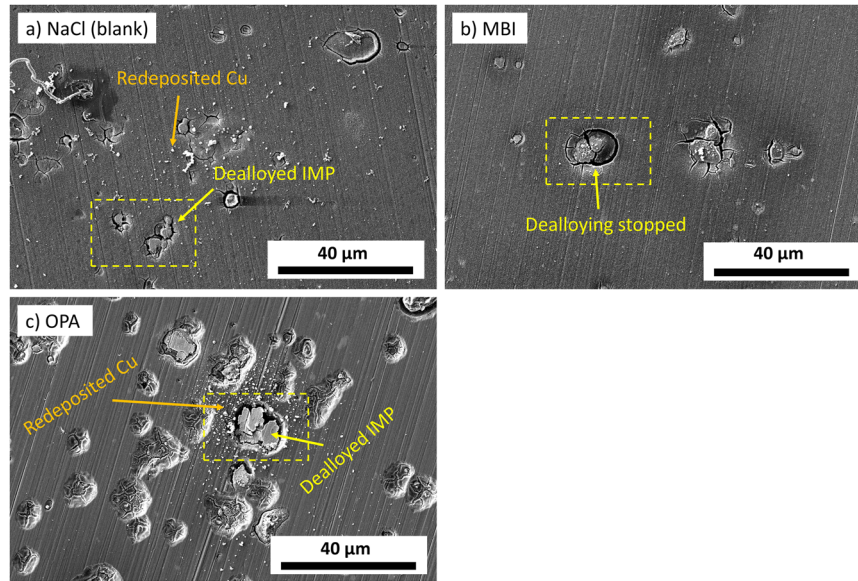


Fig. 6 SEM images of AA2024 in NaCl with and without MBI and OPA. SEM secondary electron images for AA2024 immersed for 24 h in **a** 0.5 M NaCl solution, **b** 0.5 M NaCl containing 1 mM MBI and **c** 0.5 M NaCl containing 1 mM OPA.

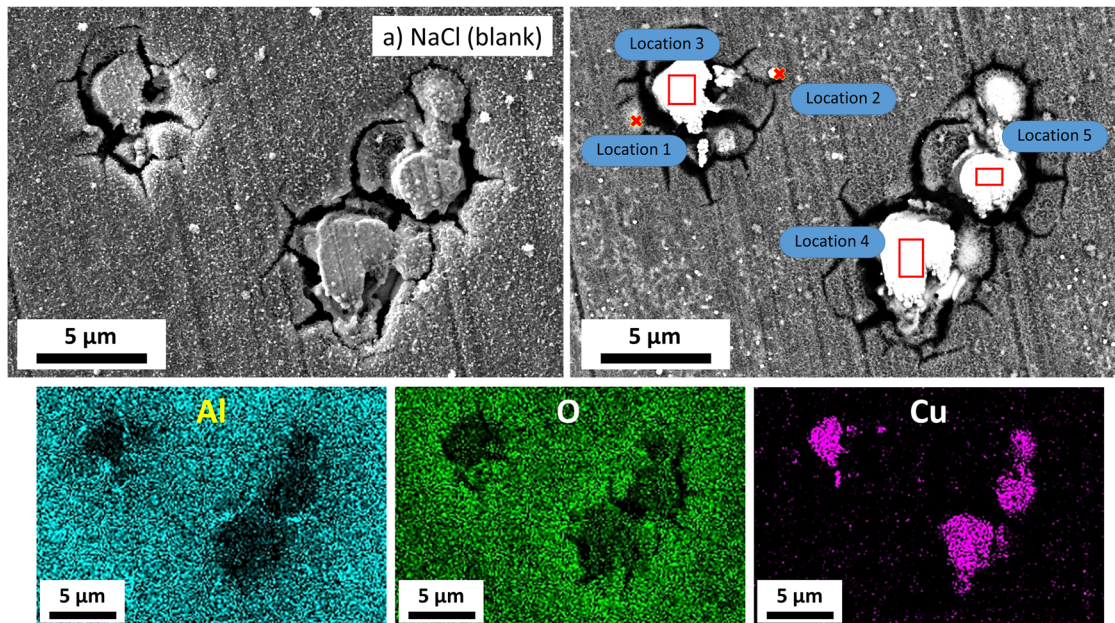


Fig. 7 SEM-EDS analysis of Al_2CuMg IMP in NaCl. SEM-EDS analysis of local corrosion induced by S-phase (Al_2CuMg) particles (in Fig. 6a) recorded in secondary electron (SE) mode (left) and back-scattered mode (right) after 24 h immersion in 0.5 M NaCl solution. Locations denoted by a cross mark, square and rectangle indicate the areas/spots where the EDS analysis was conducted (Table 1). The elements were labelled in the EDS maps.

Table 1. EDS analysis of AA2024 immersed for 24 h in NaCl. Analyses were performed at locations 1 to 5, as denoted in Fig. 7.

Location	at.% Al	at.% O	at.% Cu	at.% Fe	at.% Mg
1	25.7	51.5	19.3	3.5	–
2	3.0	7.1	89.9	–	–
3	8.9	23.4	66.8	–	0.9
4	13.0	30.6	56.4	–	–
5	15.2	31.3	52.4	–	1.1

study also reveals that the transition of the mechanism of inhibition of pure metals (Cu and Al) to alloy (AA2024) is not straightforward and requires further adjustments to achieve complete protection.

METHODS

Materials, substrate preparation and chemicals

Flat sheets of AA2024 clad, 0.5 mm thick, distributed by Kaiser Aluminum, USA, were cut into discs 15 mm in diameter. The alloy contains Cu (4.4 wt.%), Mg (1.3 wt.%), Mn (0.5 wt.%), Fe (0.3 wt.%),

Si (0.1 wt.%), and the rest is Al. The sample's surface was water-ground first with P600-grit SiC emery paper to remove the alclad layer, then further abraded with P2400- and P4000-grit, rinsed with deionised water, and ultrasonically cleaned in absolute ethanol. The chemicals utilised for AA2024 modification were sodium chloride (NaCl, purity 99.5%, supplied by Fisher Scientific), 2-mercaptobenzimidazole (MBI, purity 98%, supplied by Sigma Aldrich) and octylphosphonic acid (OPA, purity 98%, supplied by Ark Pharm, Inc.).

The molecular formula of MBI is $C_7H_6N_2S$; it is a planar organosulfur azole derivative with a $C=S$ (thione) double bond (in aqueous solutions). MBI involves two N atoms in the ring and an S atom in the thiocarbonyl group available for coordination. The molecular formula of OPA is $C_8H_{19}O_3P$. The OPA is an organophosphorus compound containing $C-PO(OR)_2$ groups (where R = alkyl, aryl or hydrogen). Structural formulae of MBI and OPA are given in Supplementary Fig. 5.

SVET instrumentation and experimental procedure

The scanning vibrating electrode instrumentation was manufactured by Applicable Electronics Inc. (Forestdale, MA, USA). The

vibrating probe consisted of Pt/Ir (80%/20%) wires, insulated with the parylene C[®] except at the tip, which was platinised to produce a spherical platinum black deposit at the tip with a diameter of 20 μm , which served as a sensor. Two Pt wires were employed as signal and reference electrodes. Mapping of electrochemical activity was performed in a constant height regime with a mean distance between the microelectrode and the sample surface of 100 μm . A video camera connected to an optical microscope was introduced in the system both for determining the tip-sample distance and for monitoring the movement of the vibrating electrode over the sample during operation, recording images of the substrate surface in real time. The measurements were made with the electrode tip vibrating perpendicular and parallel to the sample embedded horizontally in the epoxy resin and facing upwards. Microelectrochemical measurements were performed at room temperature under naturally aerated conditions in either 10 mM NaCl-containing 1 mM MBI or OPA inhibitors or just 10 mM NaCl solution. In-situ measurements of the corrosion inhibition consisted of two stages: first, the measuring cell was filled with 1 mM MBI or OPA + 10 mM NaCl solution (i.e., with an inhibitor reservoir) for 24 h, and then the solution was replaced by 10 mM

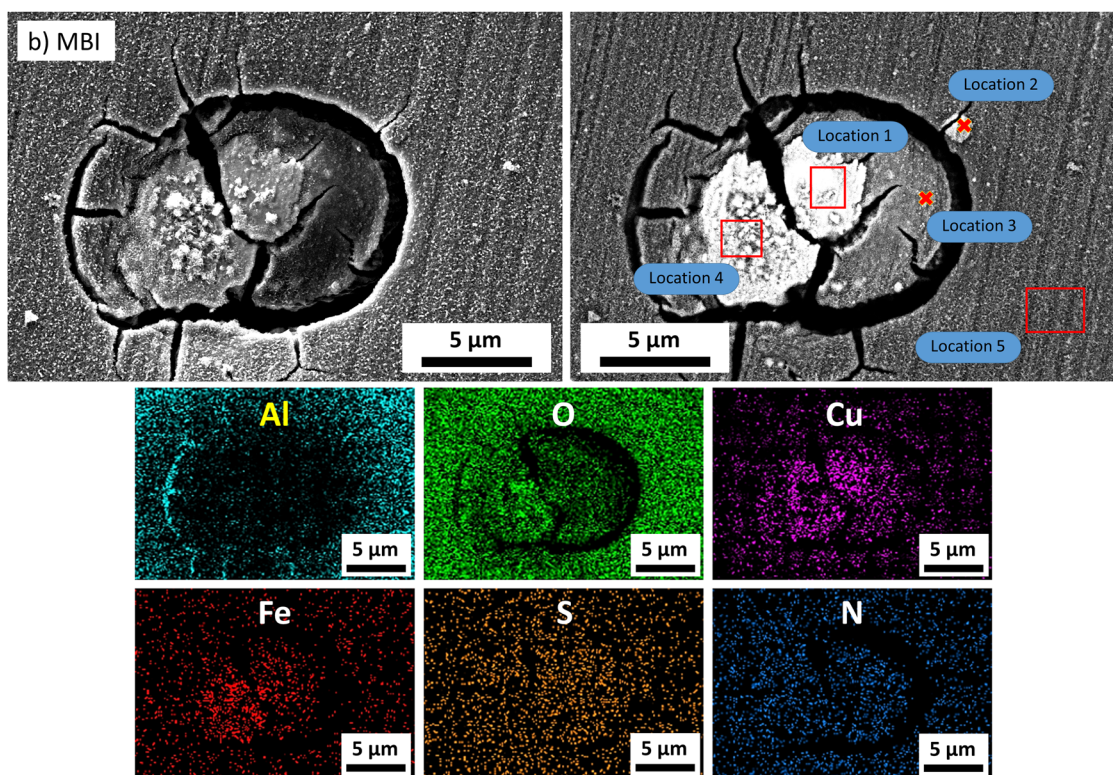


Fig. 8 SEM-EDS analysis of Al_7Cu_2Fe IMP in NaCl + MBI. SEM-EDS analysis of local corrosion induced by Al_7Cu_2Fe particle (in Fig. 6b) recorded in secondary electron (SE) mode (left) and back-scattered mode (right) after 24 h immersion in 0.5 M NaCl solution containing 1 mM MBI. Locations denoted by a cross mark, square and rectangle indicate the spots where the EDS analysis was conducted (Table 2). The elements were labelled in the EDS maps.

Location	at.% Al	at.% O	at.% Cu	at.% S	at.% N	at.% Fe	at.% Mg
1	8.2	31.2	28.2	13.8	11.1	7.6	–
2	19.9	48.2	11.9	7.0	6.1	6.9	–
3	13.8	32.6	16.0	18.2	19.4	–	–
4	11.9	39.4	16.3	8.9	8.1	15.4	–
5	54.7	40.0	2.5	2.3	–	–	0.6

NaCl (i.e., without inhibitor reservoir) for 12 h. The electrochemical activity was monitored throughout the immersion period. In addition, the corrosion of a control sample (blank) was monitored

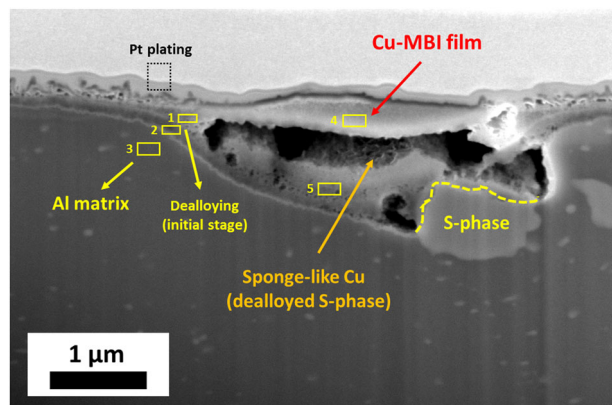


Fig. 9 Cross-section analysis of Al_2CuMg IMP in $\text{NaCl} + \text{MBI}$. FIB-SEM (cross-section) analysis of local corrosion induced by Al_2CuMg phase after 24 h immersion of AA2024 in 0.5 M NaCl containing 1 mM MBI. Yellow horizontal rectangles denote spots where the EDS analysis was performed (Table 3). Top-view of the particle is given in Supplementary Fig. 4.

Table 3. EDS analysis of AA2024 immersed for 24 h in $\text{MBI} + \text{NaCl}$. Analyses were performed at locations 1 to 5, as denoted in Fig. 9. The results are presented as atomic percentages (at.%).

Location	Al	O	Cu	Mg	S	N	Cl	Si
1	65.4	27.7	4.2	0.9	–	–	–	1.8
2	64.9	25.6	3.2	0.5	3.8	–	1.1	0.9
3	92.5	4.5	1.7	1.3	–	–	–	–
4	8.2	23.1	38.6	0.9	10.7	5.1	3.4	–
5	49.4	31.9	6.2	0.4	7.0	3.5	1.1	0.5

in 10 mM NaCl for 12 h. The 1 mM inhibitor concentration was selected to align with our previous studies on Al and Cu with and without galvanic coupling^{13–15,18}.

Conventional electrochemical measurements

Electrochemical measurements were carried out in a conventional three-electrode cell assembly using PGSTAT M204 Autolab (Metrohm, Utrecht, Netherlands) multichannel potentiostat/galvanostat controlled by NOVA software. The working electrode (WE) was an AA2024 disc with a 1 cm^2 exposed surface area. A Pt mesh and an $\text{Ag}/\text{AgCl}_{\text{sat.}}$ (+0.197 V vs. standard hydrogen electrode) were employed as the counter and reference electrodes, respectively. The latter was used with a Luggin capillary to minimise IR drops at the WE surface. The polarisation curves were recorded starting in the cathodic range 250 mV below E_{OCP} and increasing the potential in the anodic direction until reaching the cut-off ionic current density of 10^{-3} A cm^{-2} at a scan rate of 1 mV s^{-1} . All electrochemical measurements were carried out at 298 K in NaCl solution containing inhibitor, except the blank solution containing only 0.5 M NaCl.

SEM-EDS-FIB characterisation

Scanning electron microscopy combined with energy-dispersive X-ray spectroscopy (SEM-EDS) was applied to reveal the morphology and semi-quantitative composition of the surface at areas of interest. SEM images were recorded in secondary electron (SE) and back-scattered electron (BSE) imaging modes at beam energies of 5 keV and 15 keV, respectively, using a field emission (FE) SEM JSM 7600 F, JEOL, Japan, equipped with EDS (Inca Oxford 350 EDS SDD). Before analysis, the samples were coated with a thin carbon layer to reduce the charging effect.

Focused ion beam microscopy (FIB) coupled with EDS revealed the composition and thickness of layers at the cross-section of the S phase (Al_2CuMg) particle on the AA2024 substrate. First, an FEI Helios Nanolab 650 microscope, equipped with EDS (Oxford Instruments Aztec system with X-max SDD detector), was employed to deposit two Pt protection layers – electron-beam-assisted and ion beam (Ga^+)-assisted ones with thicknesses of 0.2 and 1 μm , respectively. A trench was then opened by milling under rough conditions with Ga^+ ions of 2.5 nA at 30 kV, followed

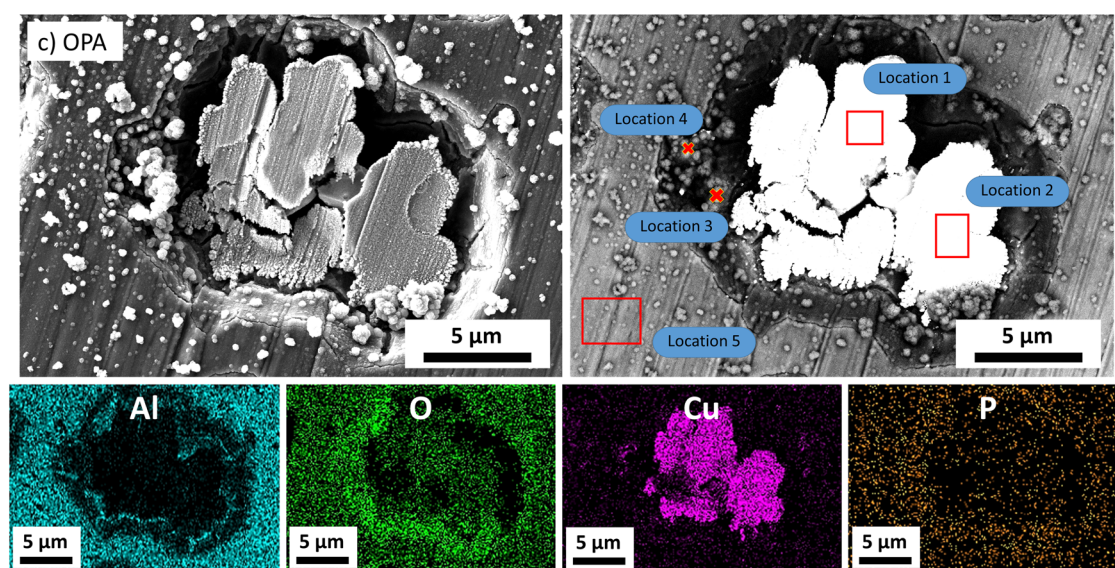


Fig. 10 SEM-EDS analysis of Al_2CuMg IMP in $\text{NaCl} + \text{OPA}$. SEM-EDS analysis of local corrosion induced by S-phase (Al_2CuMg) particles (in Fig. 6c) recorded in secondary electron (SE) mode (left) and back-scattered mode (right) after 24 h immersion in 0.5 M NaCl containing 1 mM OPA. Locations denoted by a cross mark, square and rectangle indicate the spots where the EDS analysis was conducted (Table 4). The elements were labelled in the EDS maps. The Mg map was not shown because Mg is present only in the matrix.

Table 4. EDS analysis of AA2024 immersed for 24 h in OPA+NaCl. Analyses were performed at locations 1 to 5, as denoted in Fig. 10.

Location	at.% Al	at.% O	at.% Cu	at.% P	at.% Mg
1	6.8	18.5	74.8	–	–
2	5.1	15.9	79.1	–	–
3	17.2	59.8	4.3	18.7	–
4	11.2	31.8	54.2	2.8	–
5	78.1	15.9	1.4	3.4	1.2

by rough polishing (0.77 nA, 30 kV) and fine polishing (0.4 nA, 30 kV). Within the trench, the cross-section across the S-phase and the substrate was analysed by SEM-EDS.

DATA AVAILABILITY

The data generated and analysed during the current study are available from the corresponding author upon reasonable request.

Received: 22 January 2023; Accepted: 23 May 2023;

Published online: 04 July 2023

REFERENCES

- Prasad, N. & Wanhill, R. *Aerospace Materials and Material Technologies*. (Springer, 2017).
- Frankel, G. S. Pitting Corrosion of Metals: A Review of the Critical Factors. *J. Electrochem. Soc.* **145**, 2186–2198 (1998).
- Buchheit, R. G., Grant, R. P., Hlava, P. F., Mckenzie, B. & Zender, G. L. Local Dissolution Phenomena Associated with S Phase (Al_2CuMg) Particles in Aluminum Alloy 2024-T3. *J. Electrochem. Soc.* **144**, 2621–2628 (1997).
- Buchheit, R. G., Martinez, M. A. & Montes, L. P. Evidence for Cu ion formation by dissolution and dealloying the Al_2CuMg intermetallic compound in rotating ring-disk collection experiments. *J. Electrochem. Soc.* **141**, 119–124 (2000).
- Obispo, H. M., Murr, L. E., Arrowood, R. M. & Trillo, E. A. Copper deposition during the corrosion of aluminum alloy 2024 in sodium chloride solutions. *J. Mater. Sci.* **35**, 3479–3495 (2000).
- Chen, G. S., Gao, M. & Wei, R. P. Microconstituent-Induced Pitting Corrosion in Aluminum Alloy 2024-T3. *Corros* **52**, 8–15 (1996).
- Hashimoto, T. et al. Investigation of dealloying of S phase (Al_2CuMg) in AA 2024-T3 aluminium alloy using high resolution 2D and 3D electron imaging. *Corros. Sci.* **103**, 157–164 (2016).
- Vukmirovic, M. B., Vasiljevic, N., Dimitrov, N. & Sieradzki, K. Diffusion-Limited Current Density of Oxygen Reduction on Copper. *J. Electrochem. Soc.* **150**, B10–B15 (2003).
- Jakab, M. A., Little, D. A. & Scully, J. R. Experimental and modeling studies of the oxygen reduction reaction on AA2024-T3. *J. Electrochem. Soc.* **152**, B311–B320 (2005).
- Boag, A. et al. Stable pit formation on AA2024-T3 in a NaCl environment. *Corros. Sci.* **52**, 90–103 (2010).
- Glenn, A. M. et al. Corrosion of AA2024-T3 Part III: Propagation. *Corros. Sci.* **53**, 40–50 (2011).
- Sastri, V. S. *Green Corrosion Inhibitors: Theory and Practice*. *Green Corrosion Inhibitors: Theory and Practice* (John Wiley & Sons, 2011). <https://doi.org/10.1002/9781118015438>.
- Kozlica, D. K. & Milošev, I. Corrosion inhibition of copper and aluminium by 2-mercaptobenzimidazole and octylphosphonic acid—Surface pre-treatment and method of film preparation. *Electrochim. Acta* **431**, 141154 (2022).
- Kozlica, D. K., Kokalj, A. & Milošev, I. Synergistic effect of 2-mercaptobenzimidazole and octylphosphonic acid as corrosion inhibitors for copper and aluminium – An electrochemical, XPS, FTIR and DFT study. *Corros. Sci.* **182**, 109082 (2021).
- Kozlica, D. K., Ekar, J., Kovač, J. & Milošev, I. Roles of chloride ions in the formation of corrosion protective films on copper. *J. Electrochem. Soc.* **168**, 031504 (2021).
- Bastos, A. C., Quevedo, M. C., Karavai, O. V. & Ferreira, M. G. S. Review—On the application of the scanning vibrating electrode technique (SVET) to corrosion research. *J. Electrochem. Soc.* **164**, C973–C990 (2017).
- Jadhav, N. & Gelling, V. J. Review—The Use of Localised Electrochemical Techniques for Corrosion Studies. *J. Electrochem. Soc.* **166**, C3461–C3476 (2019).

- Kozlica, D. K., Hernández-Concepción, B., Izquierdo, J., Souto, R. M. & Milošev, I. In situ, real-time imaging of redox-active species on Al/Cu galvanic couple and corrosion inhibition with 2-mercaptobenzimidazole and octylphosphonic acid. *Corros. Sci.* **217**, 111114 (2023).
- Lamaka, S. V., Zheludkevich, M. L., Yasakau, K. A., Montemor, M. F. & Ferreira, M. G. S. High effective organic corrosion inhibitors for 2024 aluminium alloy. *Electrochim. Acta* **52**, 7231–7247 (2007).
- Marcelin, S. & Pébère, N. Synergistic effect between 8-hydroxyquinoline and benzotriazole for the corrosion protection of 2024 aluminium alloy: A local electrochemical impedance approach. *Corros. Sci.* **101**, 66–74 (2015).
- Williams, G., Coleman, A. J. & McMurray, H. N. Inhibition of Aluminium Alloy AA2024-T3 pitting corrosion by copper complexing compounds. *Electrochim. Acta* **55**, 5947–5958 (2010).
- Kosari, A. et al. Dealloying-driven local corrosion by intermetallic constituent particles and dispersoids in aerospace aluminium alloys. *Corros. Sci.* **177**, 108947 (2020).
- Milošev, I., Kapun, B. & Rodič, P. The Relation Between the Microstructure of Aluminum Alloy 7075-T6 and the Type of Cerium Salt in the Formation of the Cerium Conversion Layer. *J. Electrochem. Soc.* **9**, 091501 (2022).
- Olgiati, M., Denissen, P. J. & Garcia, S. J. When all intermetallics dealloy in AA2024-T3: Quantifying early stage intermetallic corrosion kinetics under immersion. *Corros. Sci.* **192**, 109836 (2021).
- Burstein, G. T., Liu, C., Souto, R. M. & Vines, S. P. Origins of pitting corrosion. *Corros. Eng. Sci. Technol.* **39**, 25–30 (2004).
- Xue, G., Huang, X. Y., Dong, J. & Zhang, J. The formation of an effective anti-corrosion film on copper surfaces from 2-mercaptobenzimidazole solution. *J. Electroanal. Chem.* **310**, 139–148 (1991).
- Finšgar, M. 2-Mercaptobenzimidazole as a copper corrosion inhibitor: Part I. Long-term immersion, 3D-profilometry, and electrochemistry. *Corros. Sci.* **72**, 82–89 (2013).
- Finšgar, M. 2-Mercaptobenzimidazole as a copper corrosion inhibitor: Part II. Surface analysis using X-ray photoelectron spectroscopy. *Corros. Sci.* **72**, 90–98 (2013).
- Milošev, I., Kovačević, N., Kovač, J. & Kokalj, A. The roles of mercapto, benzene and methyl groups in the corrosion inhibition of imidazoles on copper: I. Experimental characterisation. *Corros. Sci.* **98**, 107–118 (2015).
- Kovačević, N., Milošev, I. & Kokalj, A. The roles of mercapto, benzene, and methyl groups in the corrosion inhibition of imidazoles on copper: II. Inhibitor–copper bonding. *Corros. Sci.* **98**, 457–470 (2015).
- Chadwick, D. & Hashemi, T. Electron spectroscopy of corrosion inhibitors: Surface films formed by 2-mercaptobenzothiazole and 2-mercaptobenzimidazole on copper. *Surf. Sci.* **89**, 649–659 (1979).
- Izquierdo, J., Santana, J. J., González, S. & Souto, R. M. Scanning microelectrochemical characterization of the anti-corrosion performance of inhibitor films formed by 2-mercaptobenzimidazole on copper. *Prog. Org. Coat.* **74**, 526–533 (2012).
- Milošev, I. et al. Editors' Choice—The Effect of Anchor Group and Alkyl Backbone Chain on Performance of Organic Compounds as Corrosion Inhibitors for Aluminium Investigated Using an Integrative Experimental-Modeling Approach. *J. Electrochem. Soc.* **167**, 61509 (2020).

ACKNOWLEDGEMENTS

The Ph.D. scholarship for D.K.K. by Ad Futura through the Public scholarship, development, disability and maintenance fund of the Republic of Slovenia is acknowledged. D.K.K. also expresses his gratitude to the ERASMUS+ traineeship program for financially supporting a 3-month mobility grant to the University of La Laguna, Tenerife, Spain, during his doctoral studies. Funding by the Slovenian Research Agency (research core funding grants no. P2-0393 and P1-0134), and by the Spanish Ministry of Science and Innovation (MICINN, Madrid, Spain) and the European Regional Development Fund (Brussels, Belgium) MCIN/AEI/10.13039/501100011033/FEDER/UE under grant PID2021-127445NB-I00 are also acknowledged. The authors acknowledge Barbara Kapun, BSc, of the Jožef Stefan Institute for her valuable contribution by performing the FIB-SEM-EDS analyses and Center of Excellence - Nanocenter for the use of FIB-SEM-EDS equipment.

AUTHOR CONTRIBUTIONS

D.K.K.: Measurements, conceptualisation, data analysis, visualisation, methodology, writing; J.I.: conceptualisation, methodology, writing; R.M.S.: conceptualisation, methodology, writing, funding acquisition; I.M.: conceptualisation, methodology, writing, funding acquisition.

COMPETING INTERESTS

The authors declare no competing interests.

ADDITIONAL INFORMATION

Supplementary information The online version contains supplementary material available at <https://doi.org/10.1038/s41529-023-00368-z>.

Correspondence and requests for materials should be addressed to Ricardo M. Souto or Ingrid Milošev.

Reprints and permission information is available at <http://www.nature.com/reprints>

Publisher's note Springer Nature remains neutral with regard to jurisdictional claims in published maps and institutional affiliations.



Open Access This article is licensed under a Creative Commons Attribution 4.0 International License, which permits use, sharing, adaptation, distribution and reproduction in any medium or format, as long as you give appropriate credit to the original author(s) and the source, provide a link to the Creative Commons license, and indicate if changes were made. The images or other third party material in this article are included in the article's Creative Commons license, unless indicated otherwise in a credit line to the material. If material is not included in the article's Creative Commons license and your intended use is not permitted by statutory regulation or exceeds the permitted use, you will need to obtain permission directly from the copyright holder. To view a copy of this license, visit <http://creativecommons.org/licenses/by/4.0/>.

© The Author(s) 2023